In Situ, Fast, High-Temperature Synthesis of Nickel Nanoparticles in Reduced Graphene Oxide Matrix

*Yiju Li, Yanan Chen, Anmin Nie, Aijiang Lu, Rohit Jiji Jacob, Tingting Gao, Jianwei Song, Jiaqi Dai, Jiayu Wan, Glenn Pastel, Michael R. Zachariah, Reza Shahbazian Yassar, and Liangbing Hu**

For the first time, a fast heating–cooling process is reported for the synthesis of carbon-coated nickel (Ni) nanoparticles on a reduced graphene oxide (RGO) matrix (nano-Ni@C/RGO) as a high-performance H_2O_2 fuel catalyst. The Joule heating temperature can reach up to ≈2400 K and the heating time can be less than 0.1 s. Ni microparticles with an average diameter of 2 µm can be directly converted into nanoparticles with an average diameter of 75 nm. The Ni nanoparticles embedded in RGO are evaluated for electro-oxidation performance as a H_2O_2 fuel in a direct peroxide–peroxide fuel cell, which exhibits an electro-oxidation current density of 602 mA cm^{-2} at 0.2 V (vs Ag/AgCl), ≈150 times higher than the original Ni microparticles embedded in the RGO matrix (micro-Ni/RGO). The high-temperature, fast Joule heating process also leads to a 4–5 nm conformal carbon coating on the surface of the Ni nanoparticles, which anchors them to the RGO nanosheets and leads to an excellent catalytic stability. The newly developed nano-Ni@C/RGO composites by Joule heating hold great promise for a range of emerging energy applications, including the advanced anode materials of fuel cells.

1. Introduction

Over the past few decades, fuel cells as a type of static energy conversion device have attracted tremendous attention owing to their high electrochemical conversion efficiency, controlled emissions, and good reliability.[1–3] However, these devices suffer from a myriad of challenges such as high cost, low efficiency relative to fossil fuels, and high operating temperatures. The direct peroxide–peroxide fuel cell (DPPFC) utilizes hydrogen peroxide (H_2O_2) both as an affordable fuel at the anode and an oxidant at the cathode,[4–6] which can largely reduce the cost and enhance the feasibility of DPPFC. H_2O_2 possesses faster kinetic characteristics with two-electron transfer than alternative fuels and has no poisonous intermediates or by-products during the electro-oxidation process.[7] Additionally, the electro-oxidation production of oxygen at the anode electrode is favorable for anaerobic operating environments, such as underwater power sources. Therefore, research into high-performance materials for H_2O_2 electro-oxidation has received significant attention in the field of electrochemical catalysis.[8–10]

Recently, various types of noble catalysts have been investigated for high-efficiency electro-oxidation of H_2O_2, such as platinum (Pt), palladium (Pd), gold (Au), silver (Ag), and their alloys.[11–15] However, the inherent scarcity and expensive nature of these noble metals limit their use in extensive applications. As low-cost alternatives, some transition metals, such as cobalt (Co) and nickel (Ni), have been rigorously explored as catalysts for the electro-oxidation of H_2O_2.[16,17] The relatively low catalytic performance of these metals in an undeveloped state restricts their utilization in the field of electrocatalysis. Nanostructures can offer a higher specific surface area and expose more active sites for effective electrocatalysis, which is indicated in recent research on nanoparticles, nanosheets, nanorods, nanobelts, and nanowires.[18–22] However, the existence of a binder in an electrode nanostructure reduces the electrical conductivity and blocks some of the catalytically active sites, which can result in poor performance. Binders can also gradually degrade during the electrocatalytic reaction, which can lead to the undesirable detachment of active material from the electrode. Therefore, designing a high electroactive surface area nanostructure on a highly conductive matrix without an inactive binder is highly desirable for high-efficiency H_2O_2 electro-oxidation.

Nanoparticles hosted in a carbon matrix such as carbon nanotubes and graphene have been widely reported for high-performance energy applications.[23–31] Herein, for the first time, we report an ultrafast, high-temperature, and in situ synthetic approach to convert ≈2 µm Ni microparticles into ≈75 nm nanoparticles in a freestanding reduced graphene oxide

---

Y. Li, Y. Chen, Prof. A. Lu, T. Gao, J. Song, J. Dai,
Dr. J. Wan, G. Pastel, Prof. L. Hu
Department of Materials Science and Engineering
University of Maryland College Park
College Park, MD 20742, USA
E-mail: binghu@umd.edu

Dr. A. Nie, Prof. R. S. Yassar
Department of Mechanical and Industrial Engineering
University of Illinois at Chicago
Chicago, IL 60607, USA

R. J. Jacob, Prof. M. R. Zachariah
Department of Chemical Engineering
University of Maryland College Park
College Park, MD 20742, USA

DOI: 10.1002/aenm.201601783

(RGO) film through transient Joule heating treatment. After the treatment, the Ni nanoparticles are encapsulated within a few layers of carbon and homogenously anchored on the surface of RGO nanosheets (nano-Ni@C/RGO). The thin carbon-coated nanosized Ni particles have a high degree of exposed catalytic sites on the carbon shell and improve the charge transfer capability, which greatly enhances the H_2O_2 electro-oxidation performance.[32] Moreover, the well-defined carbon coating protects the Ni nanoparticles from destabilizing bubbles during the process of oxygen generation. The strong bond between the carbon-coated Ni nanoparticles and the RGO nanosheets leads to excellent catalytic stability and, consequently, better electrocatalytic performance than the initial Ni microparticle/RGO composite electrode (micro-Ni/RGO).

2 Results and Discussion

The carbon-encapsulated Ni nanoparticles are formed in situ through an ultrafast (60 ms) and high-temperature (≈2370 K) Joule heating method. The resulting Ni nanoparticles are uniformly distributed on the surfaces between the RGO nanosheets without agglomeration, as seen in **Figure 1**, which is attributed to the "trapping effect" of the RGO defects as a heterogeneous nucleation site. Conceptually, the Ni microparticles melt when the composite film is heated above the melting temperature (≈1730 K) to ≈2370 K for less than 0.1 s and then self-assemble into nanosized clusters on the RGO surface. When the composite film is suddenly cooled down by removing the applied current, the molten Ni will cool into nanoparticles without agglomeration at the sites of residual oxygen groups and vacancy defects. Simultaneously, a thin layer of carbon is formed on the surface of the Ni nanoparticles during the Joule heating treatment due to the catalytic effect of Ni.

The array of Ni nanoparticles with a thin carbon coating in an RGO matrix can be adapted for a range of energy applications, including batteries, fuel cell, and water splitting. We focus on adapting this innovation for DPPFC as a proof of concept because of the pressing need for affordable, high-performance catalysts. The Ni microparticle and graphene oxide composite film was first prepared by a facile filtration procedure and then preannealed in an argon atmosphere to obtain the freestanding micro-Ni/RGO thin film. The freestanding micro-Ni/RGO composite film is suspended on a concave glass holder and placed into a vacuum chamber (Figure S1, Supporting Information) before applying a direct current to rapidly heat the composite film as displayed in **Figure 2**a,b. The ultrafast nature of the Joule heating process induces a thermal shock on the composite film that is carefully monitored by a spectropyrometer and a 32 channel photomultiplier (PMT) (Figure 2c). The time-resolved intensities on the first 27 channels with corresponding wavelengths of 513–858 nm were acquired at a rate of 10 kHz to provide spectral information of the ultrafast heating event (Figure 2d). The intensity peaks occur within the 12 ms time frame and gradually drop in spite of the electrical load still being supplied to the film. The time-resolved spectra were used to extract the temperature by fitting to Planck's law with Grey body assumption and the temperature curve is shown in Figure 2e and accompanied by the intensity profile on the 858 nm channel. The observed temperature rise follows the intensity profile, and there is no appreciable reduction in temperature until 45 ms after the load is first applied. Once the power supply was cut off, the sample was fast cooled down in roughly 5 ms via thermal conduction to the holder and radiation to the surroundings in vacuum chamber. The time for the temperature to rise and cool is estimated as 12 and 5 ms, respectively. The highest temperature achieved by the nano-Ni@C/RGO sample is around 2370 K during the ultrafast Joule heating process.

The electrical conductivity of the micro-Ni/RGO composite film before and after fast Joule heating is obtained by a linear fit of the two-probe *I*–*V* curves. Two copper probes are separately attached to the edges of the film using colloidal silver paste and the dimensions of the tested sample are 0.5 cm (width) × 1.0 cm (length) × 70 µm (thickness). The typical *I*–*V* curves are displayed in Figure 2f. The conductance of micro-Ni/RGO

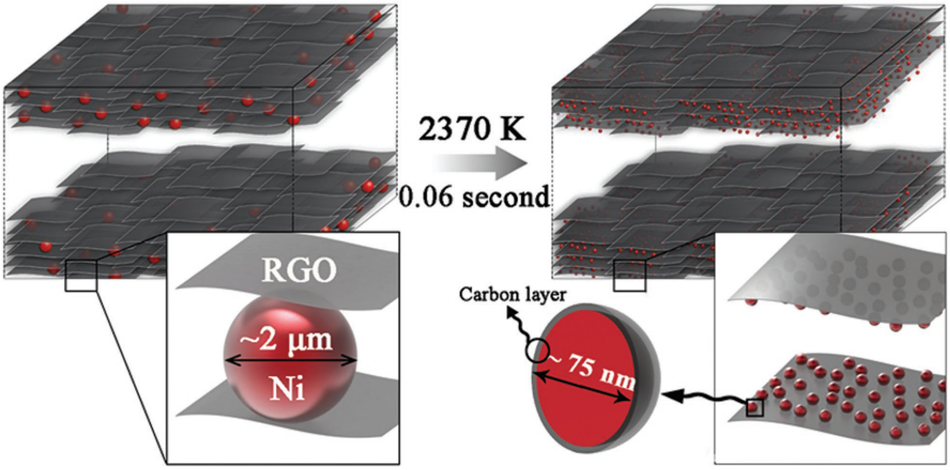

Figure 1. Schematic of the ultrafast synthesis of Ni nanoparticles encapsulated in carbon layers on RGO nanosheets. When the Ni microparticles hosted in the RGO matrix are heated to ≈2370 K for ≈0.06 s, they reassemble into nanoparticles with an average diameter of ≈75 nm and a thin, uniform carbon coating.

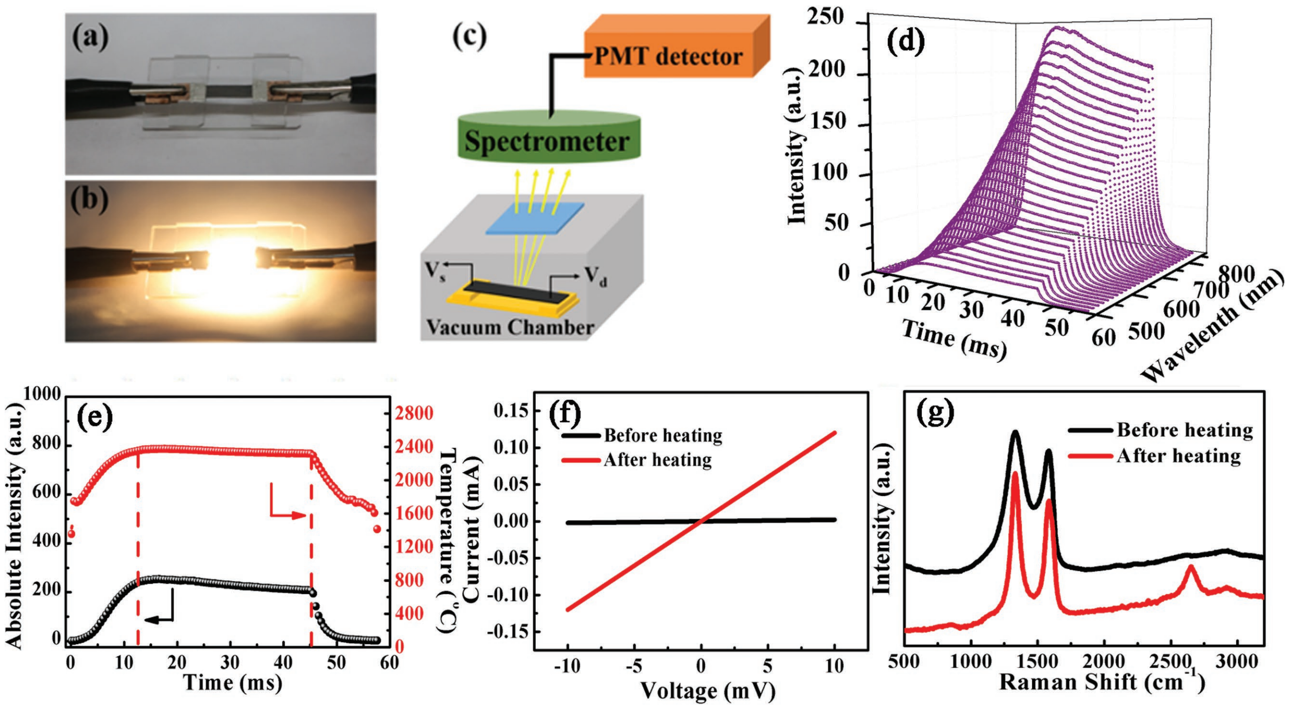

Figure 2. a,b) Digital photographs of the Joule heating device with a suspended micro-Ni/RGO composite freestanding film on a home-made glass substrate before and during heat treatment. c) Schematic of the optical measurements for spectral radiance detection in a vacuum chamber with a spectrometer and PMT detector. d) High speed, 10 kHz spectroscopic measurement of the Ni/RGO film during the Joule heating process with intensities captured over 27 channels (513–858 nm). e) Processed temperature values for the spectra along with the intensity on the 858 nm channel. Temperature is determined by fitting the spectra to Planck's law. f) *I–V* curves of the micro-Ni/RGO freestanding film before and after the Joule heating treatment. g) Raman spectra of the micro-Ni/RGO composite before and after the Joule heating treatment.

composite films tremendously increases by 83-fold, from 0.15 to 12.5 mS, after the Joule heating treatment. The enhanced conductivity is attributed to the reduction of RGO film caused by the thermal shock. The disordered nature of the micro-Ni/RGO composite before and after the ultrafast high-temperature treatment is demonstrated by Raman spectroscopy (Figure 2g). Two apparent peaks located at 1350 and 1580 cm^{-1} are assigned to the D band and the G band, respectively. The D band at 1350 cm^{-1} is indicative of structural defects and disorder in the RGO matrix while the G band identifies first-order scattering of the E_{2g} mode in sp^2 carbon domains.[33] The integrated intensity ratio of the D peak to G peak (I_D/I_G) exhibits no obvious decrease after the Joule heating treatment. The exceptional Raman result is likely related to the uniform formation of a carbon coating on the Ni nanoparticles at defect sites of the RGO nanosheets, which can retain numerous defects in RGO nanosheets.[34] It is also important to note that an obvious 2D peak at 2680 cm^{-1} emerges in the Raman spectra after Joule heating, which indicates the removal of oxygenic functional groups between the RGO interlayers and formation of certain stacked structures. After elimination of some oxygenic groups, the carbon atoms with dangling bonds can facilitate the interlayer bridging bond formation during the high-temperature treatment. This results in a RGO film with high conductivity and good mechanical strength for DPPFC applications.[35]

In order to investigate the morphology of in situ formed Ni nanoparticles inside RGO films, we conducted scanning electron microscopy (SEM) and transmission electron microscopy (TEM). The vacuum filtrated graphene oxide (GO) and Ni microparticles composite film (micro-Ni/GO) with a thickness of 90 µm (Figure S2c, Supporting Information) was flexible (Figure S2a,b, Supporting Information). Ni microparticles are distributed uniformly inside the GO nanosheet matrix (Figure S2d,e, Supporting Information). After preannealing under argon atmosphere at 300 °C, the reduced GO is electrically conductive. As shown in **Figure 3**a, the Ni microparticles are still randomly dispersed in the RGO matrix and range in size from 1 to 4 µm with an average diameter of ≈2 µm. After fast Joule heating, the Ni microparticles are transformed into nanoparticles with a diameter between 25 and 100 nm that are homogenously distributed and anchored on the surface of the RGO nanosheets (Figure 3b,c). To further reveal the inner morphology of the composite film, we mechanically exfoliated the top layers with scotch tape to expose the inner part of the composite. The morphology of the micro-Ni/RGO film before and after fast Joule heating is shown in Figure S3 (Supporting Information). It can be observed that the Ni nanoparticles were also uniformly dispersed without agglomeration inside the RGO film. An high angle annular dark field-scaning transmission electron microscopy (HAADF-STEM) image of the nano-Ni@C/RGO composite further confirms the distribution of Ni nanoparticles (Figure 3d). Mechanical sonication while preparing the TEM sample did not detach the Ni nanoparticles from the RGO matrix, which demonstrates the strong binding between the carbon-coated Ni nanoparticles and the RGO nanosheets. Figure 3e shows the selected area electron

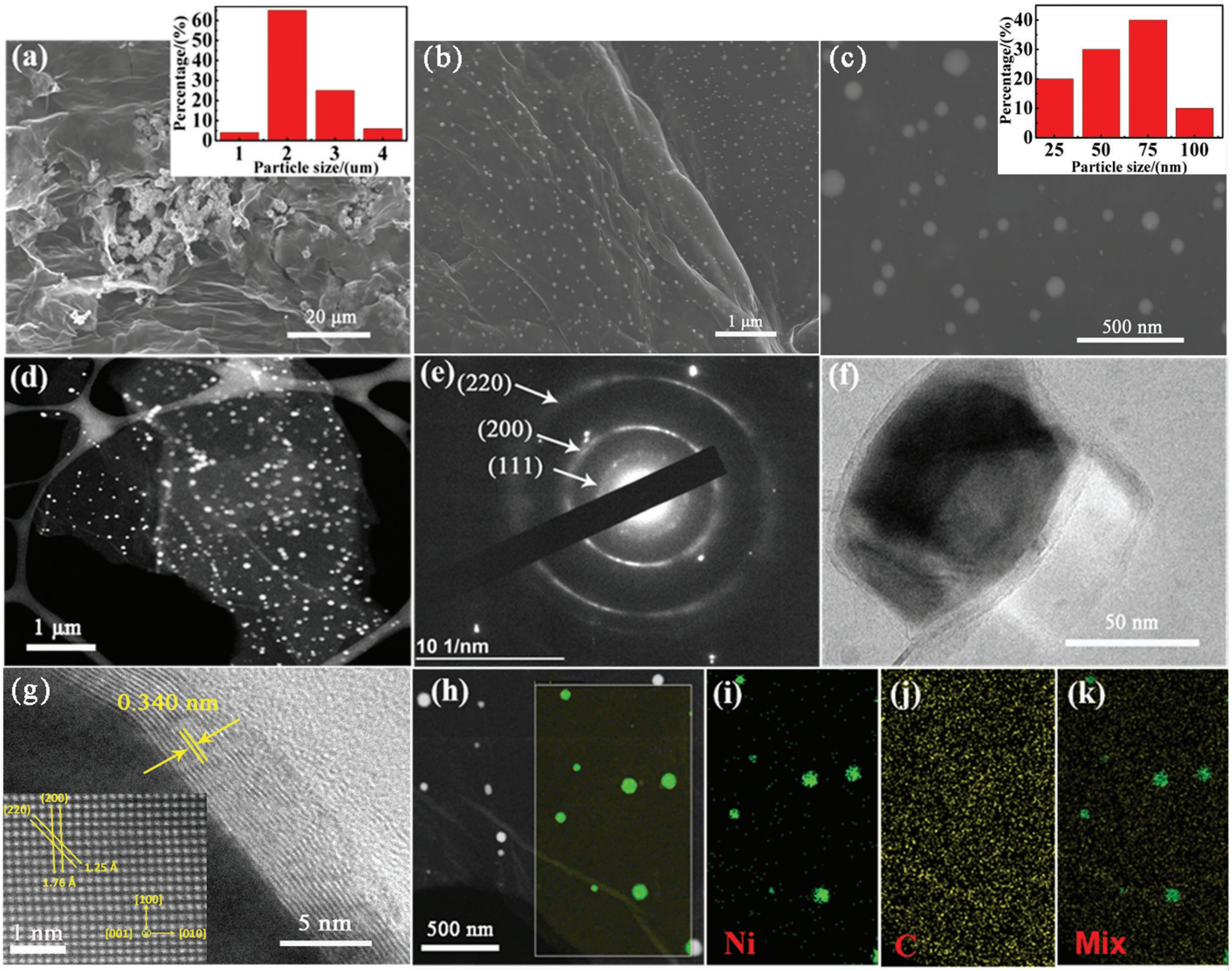

Figure 3. a) SEM image of the micro-Ni/RGO film. The inset is the particles size distribution of the Ni microparticles in the RGO film before the Joule heating treatment. b,c) SEM images of the nano-Ni@C/RGO film. The inset is the particles size distribution of the Ni nanoparticles in the RGO film after Joule heating treatment. d) HAADF-STEM image of the nano-Ni@C/RGO composite. e) SAED pattern of the nano-Ni@C/RGO composite. f) TEM image of the nano-Ni@C/RGO composite. g) HRTEM of nano-Ni@C/RGO composite. The inset is the atomic-scale HAADF-STEM image of nano-Ni@C/RGO composite. The HAADF image was taken with the [001] zone axis. h–k) HAADF-STEM image of the nano-Ni@C/RGO composite and the corresponding EDX elemental maps.

diffraction pattern (SAED) of the nano-Ni@C/RGO composite. The well-defined SAED pattern indicates the polycrystalline nature of the Ni nanoparticles, and the diffraction rings can be clearly assigned to the (220), (200), and (111) planes, respectively.[36] The TEM and HRTEM images reveal the core–shell nanostructure of the Ni nanoparticles formed by the high-temperature thermal shock (Figure 3f,g). The Ni nanoparticles are conformally coated by a 4–5 nm carbon layer, which is consistent with the result from the high-resolution HAADF-STEM (Figure S4, Supporting Information). The lattice fringes can be seen in the HRTEM image, in which 0.340 nm corresponds to the (002) plane of graphitic carbon materials.[37] The atomic scale HAADF image of the nickel nanoparticles on RGO is taken along the [001] zone axis (inset in Figure 3g). The *d*-spacing of the two crossed lattice planes is measured to be 1.76 and 1.25 Å, corresponding to the (200) and (220) planes of fcc Ni metal (Space Group: Fm3m), respectively. The HAADF-STEM image of nano-Ni@C/RGO composite and the corresponding EDX elemental maps are shown in Figure 3h–k. These results confirm the homogenous coating of the Ni nanoparticles between the RGO nanosheets.

We carried out Monte Carlo and molecular dynamics simulations to understand the Ni nanoparticle formation mechanism by the in situ high-temperature thermal shock. The Joule heating treatment in the experiments can melt the Ni microparticles and when the temperature cools down, the melted Ni self-assembles at defects sites on the basal plane of the RGO nanosheets. It was found that the Ni nanoclusters such as Ni_{38}, Ni_{55}, Ni_{92}, and Ni_{135} are stable at the high temperatures (≈2370 K) reached during the Joule heating process. **Figure 4** shows the possible formation of Ni_{92} coated with carbon and the final adsorption of the nanocluster on the RGO nanosheets based on our calculations. The carbon atoms from the defective sites on the RGO nanosheets can act as a carbon source at

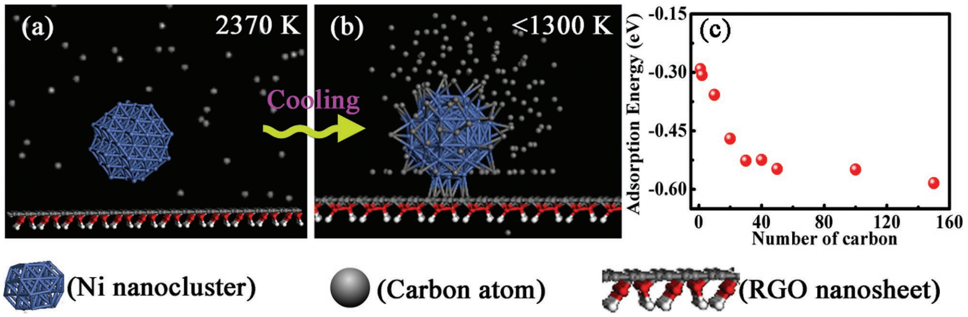

Figure 4. The modeling of formation of carbon layers on the surface of Ni nanoparticles. a) The Ni microparticles melt at high temperature (≈2370 K) and b) upon cooling, self-assemble into nanoparticles due to the defects on RGO nanosheets. Simultaneously, carbon atoms are coated on the surface of the Ni nanoclusters during the cooling process. c) The adsorption energy decreases with the increase of adsorption number of carbon.

high temperatures (Figure 4a). During the cooling process, the carbon atoms are adsorbed on the Ni nanoclusters and at the same time, the nanoclusters become trapped by the defects on the RGO nanosheets (Figure 4b). The thickness of the carbon coating gradually increased as the temperature decreased. At temperatures less than ≈1300 K, the carbon coating on the Ni nanoparticles is stable. The observed decrease in adsorption energy is inversely proportional to the number of carbon atoms, which justifies the enhanced carbon encapsulation (Figure 4c). The simulation results support the formation of carbon layers encapsulating the Ni nanoparticles on the surface of RGO nanosheets.

We evaluated the electrochemical performance of as-prepared electrodes for anode materials of DPPFCs. Cyclic voltammetry (CV) was conducted in order to estimate the electroactive specific surface area (ESSA) (cm^2 cm^{-2}) of prepared electrodes. **Figure 5**a displays the cyclic voltammograms of the pure RGO, micro-Ni/RGO, and nano-Ni@C/RGO electrodes measured in a pure potassium hydroxide (KOH) solution (4 mol L^{-1}) at a scan rate of 10 mV s^{-1}. The CV curve of RGO does not show any peaks, indicating no redox reaction on the surface of pure RGO electrode. A pair of redox peaks appear on the nano-Ni@C/RGO electrode. The anodic peak at 0.36 V and the cathodic peak at 0.22 V correspond to the redox reaction

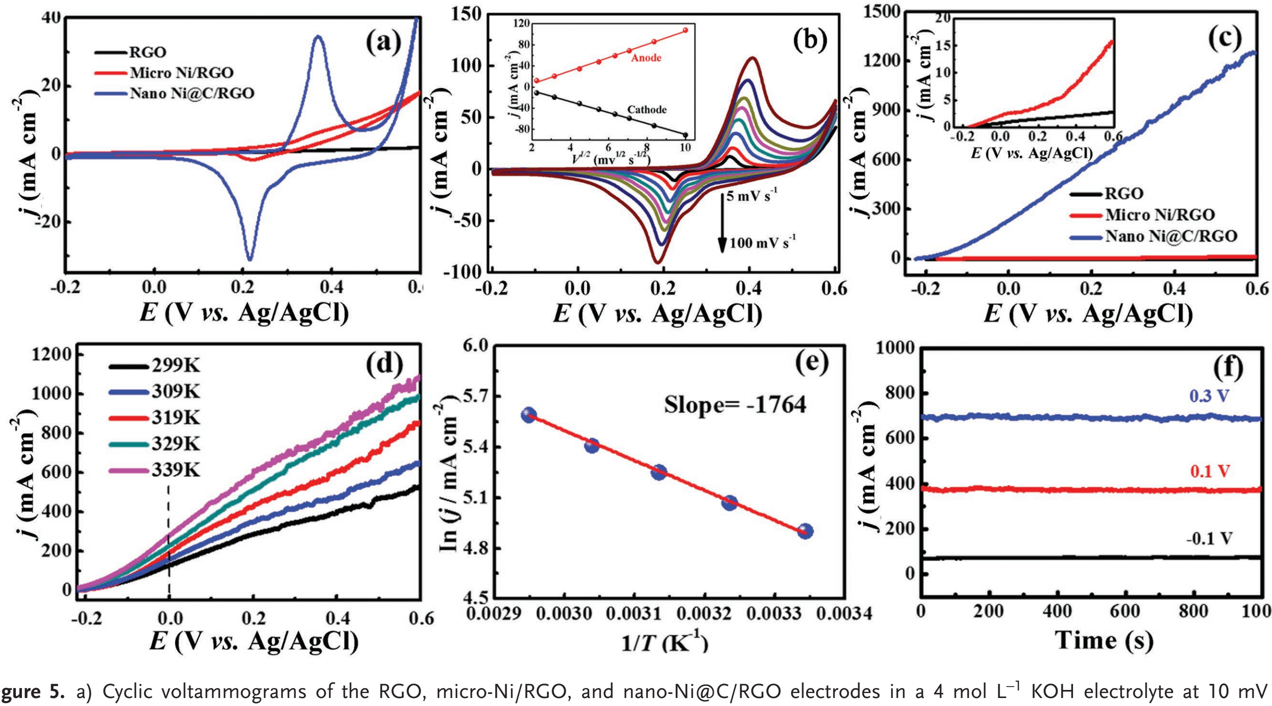

Figure 5. a) Cyclic voltammograms of the RGO, micro-Ni/RGO, and nano-Ni@C/RGO electrodes in a 4 mol L^{-1} KOH electrolyte at 10 mV s^{-1}. b) Cyclic voltammograms of the nano-Ni@C/RGO electrode in a 4 mol L^{-1} KOH electrolyte under various scan rates; the inset is the proportionality of anodic and cathodic peak currents to the square roots of scan rates. c) LSV curves of the RGO, micro-Ni/RGO, and nano-Ni@C/RGO electrodes in a 4 mol L^{-1} KOH + 0.9 mol L^{-1} H_2O_2 solution (10 mV s $^{-1}$). The inset is the enlarged curves of RGO and micro-Ni/RGO electrodes. d) LSV curves of H_2O_2 electro-oxidation of the nano-Ni@C/RGO electrode in a 2.0 mol L^{-1} KOH + 0.3 mol L^{-1} H_2O_2 solution at different temperatures (10 mV s $^{-1}$). e) Arrhenius plot of the current densities at 0 V toward H_2O_2 electro-oxidation. f) Chronoamperometric curves of the nano-Ni@C/RGO electrode for H_2O_2 electro-oxidation at different applied potentials in a 4.0 mol L^{-1} KOH + 0.9 mol L^{-1} H_2O_2 solution.

between Ni^{2+} and Ni^{3+}, respectively.[38] Analogous redox peaks for the micro-Ni/RGO electrode also show up but with a much smaller magnitude. The approximate ESSA of electrodes was calculated based on the following equation

$$\mathrm{ESSA} = Q/q \quad (1)$$

where Q (μC cm^{-2}) is the total charge that is required to reduce Ni^{3+} to Ni^{2+} and normalized by the apparent area and q represents the specific charge needed for reducing a monolayer of Ni^{3+} to Ni^{2+} on the outside surface of Ni nanoparticles. As reported in the literature, q is about 257 μC cm^{-2}.[39] The ESSA of the micro-Ni/RGO and nano-Ni@C/RGO electrodes were estimated to be 29.18 cm^2 cm^{-2} and 1245.14 cm^2 cm^{-2}, respectively. The result directly reveals the ESSA of electrode is drastically increased after the ultrafast Joule heating treatment. The small nanoparticle size enables the high utilization of surface active sites of thin carbon-coated Ni nanoparticles. Figure 5b presents typical CV curves of the nano-Ni@C/RGO electrode in a 4 mol L^{-1} KOH solution at various potential sweep rates of 5–100 mV s^{-1}. The anodic and cathodic peak current densities are both linear with the square root of the scan rates after curve fitting (inset of Figure 5b), which demonstrates the nature of fast charge transfer and the dominance of the ion diffusion controlled processes on the nano-Ni@C/RGO electrode. These properties are preferable and demonstrate the viability of this Joule heating process for producing functional and affordable nano-Ni@C/RGO electrodes for DPPFC devices.

Possibly, the H_2O_2 reacts with OH^- on the surface of the thin carbon layers through electron transfer, which is modulated by the inside Ni nanoparticles. The current density of the nano-Ni@C/RGO electrode during H_2O_2 electro-oxidation increases with the improvement of H_2O_2 and KOH concentration. The H_2O_2 reacts with the OH^- ions by a certain stoichiometric ratio during the H_2O_2 fuel electro-oxidation and too high a concentration of H_2O_2 will accelerate self-decomposition in alkaline solution, largely decreasing the efficiency of electro-oxidation. Therefore, higher H_2O_2 (>0.90 mol L^{-1}) and KOH concentrations (>4 mol L^{-1}) did not contribute to enhance the electrocatalytic performance of the H_2O_2 electro-oxidation reactions (Figures S6 and S7, Supporting Information). In our work, we selected the 4 mol L^{-1} KOH and 0.9 mol L^{-1} H_2O_2 as the optimal test solution. The compared linear sweep voltammetry (LSV) curves of H_2O_2 electro-oxidation for RGO, micro-Ni/RGO, and nano-Ni@C/RGO electrodes are displayed in Figure 5c. The onset oxidation potential represents the potential at which its corresponding electro-oxidation current density is just higher than 0 mA. The onset oxidation potential toward H_2O_2 electro-oxidation for the nano-Ni@C/RGO electrode was about –0.22 V (vs Ag/AgCl), which is a 60 mV negative shift from the micro-Ni/RGO electrode (Figure S8, Supporting Information). This is consistent with the result reported by Xiao et al. that the thin carbon layers are able to lower the onset potential.[40] The lower onset oxidation potential indicates that the reaction sites on the nano-Ni@C/RGO electrode are much more active than on the micro-Ni/RGO electrode. Moreover, the electro-oxidation current density of the nano-Ni@C/RGO electrode (602 mA cm^{-2} at 0.2 V) is nearly 147 times higher than the micro-Ni/RGO electrode (4.2 mA cm^{-2} for 0.2 V). Therefore, the nano-Ni@C/RGO electrode shows superior electrocatalytic performance toward H_2O_2 electro-oxidation in terms of the oxidation current density and onset potential. These properties are attributed to the small nanoparticle size that enables the high utilization of surface active sites and the carbon shell can accelerate the sluggish kinetics of electro-oxidation as well as the conductive substrate of RGO nanosheets.[32]

The LSV curves of H_2O_2 electro-oxidation for the nano-Ni@C/RGO electrode under five different temperatures between 299 and 339 K were measured and are shown in Figure 5d. The current density of H_2O_2 electro-oxidation increases with the elevated reaction temperature, which is supported by the Arrhenius plot in Figure 5e and the corresponding Arrhenius equation for electro-oxidation. Figure 5e shows the Arrhenius plot with the logarithm of current densities (ln j) at 0 V as the Y-axis and the reciprocal of temperature ($1/T$) as the X-axis, according to the following Arrhenius equation

$$\frac{\partial \mathrm{In} j}{\partial T} = -\frac{E_a}{RT^2} \quad (2)$$

where j is the current density at a specific potential (mA cm^{-2}), R stands for the molar gas constant (8.314 J mol^{-1} K^{-1}), T represents the thermodynamic temperature (K), and E_a is the activation energy (J mol^{-1}).[41] The activation energy for H_2O_2 electro-oxidation for the nano-Ni@C/RGO film was estimated to be 14.66 kJ mol^{-1} based on the Arrhenius equation. We have summarized the results and offered a table to compare the activation energy for H_2O_2 electro-oxidation with other recently reported fuel electro-oxidations (Table S1, Supporting Information). Our results demonstrate a significant improvement when compared with other recent reports,[23,42–47] The nano-Ni@C/RGO electrode shows superior electrocatalytic performance with fast electro-oxidation kinetics. The stability of the nano-Ni@C/RGO electrode toward H_2O_2 electro-oxidation was studied by a certain number of linear scan voltammetric cycles. As shown in Figure S9 (Supporting Information), the electro-oxidation current density of the nano-Ni@C/RGO composite electrode decreases slightly even after 500 cycles, thereby demonstrating excellent electrochemical and structural stability. Figure 5f shows chronoamperometric curves of H_2O_2 electro-oxidation at different potentials in 4 mol L^{-1} KOH and 0.9 mol L^{-1} H_2O_2 solutions. The oxidation current densities remain stable within a 1000 s test period at all the applied potentials. At a potential of 0.30 V, the slight fluctuation in current density is attributed to the disruptive O_2 bubble production and release on the surface of electrode. The stable current densities further demonstrate that the nano-Ni@C/RGO electrode has excellent cycling stability and is a potential catalyst for H_2O_2 electro-oxidation applications. The stability of the nano-Ni@C/RGO film is due to the thin carbon layer coating, which anchors the Ni nanoparticles on the RGO surface.

3. Conclusion

In this work, we demonstrated an ultrafast, high-temperature, and in situ method to convert ≈2 μm Ni microparticles into ≈75 nm nanoparticles that are trapped by defects in a RGO matrix and encapsulated in a thin, 4–5 nm carbon coating. The temperature of the composite film reaches up to ≈2370 K in a short duration of ≈0.06 s. The Ni nanoparticles are tightly anchored on the surface of RGO nanosheets and provide an ultrahigh electroactive specific surface area of 1245 cm^2 cm^{-2}. The nano-Ni@C/RGO electrode exhibits superb electro-oxidation performance for H_2O_2 fuel (602 mA cm^{-2} at 0.2 V vs Ag/AgCl), which is nearly 150 times higher than the untreated micro-Ni/RGO electrode reference results. The nano-Ni@C/RGO electrode also shows stable electro-oxidation current densities at the applied potentials, demonstrating excellent cycling performance for DPPFC applications. The newly developed nano-Ni@C/RGO film with a high electroactive specific surface area and carbon encapsulation is a promising anode material for DPPFC and the Joule heating process is both affordable and scalable. It is expected that the demonstrated novel heating method can be applied to synthesize many other kinds of nanoparticles for a broad range of applications in the field of energy conversion and storage.

4. Experimental Section

Preparation of GO Ink: The GO ink was synthesized using an improved Hummers method. 1 g natural flake graphite was dispersed in 100 mL H_2SO_4 and H_3PO_4 mixed solution (the volume ratio of H_2SO_4/H_3PO_4 is 9:1). 6 g $KMnO_4$ was slowly added into the mixture. The above solution was kept at 50 °C and then agitated for 12 h. Subsequently, the solution was cooled down to room temperature and mixed with 80 mL 5% H_2O_2. The GO was obtained through vacuum filtration, and washed using diluted HCl solution and DI water. Finally, the GO was diluted in deionized (DI) water to achieve a 3 mg mL^{-1} GO ink.

Preparation of Micro-Ni/RGO Film: The micro-Ni/RGO film was prepared by a simple filtration method. Typically, the purchased Ni microparticles (averaging 2 µm) were added into as-prepared GO ink with a weight ratio of 1:1 (48:48 mg). The obtained solution was stirred in a Tube Vertex Mixer until a uniform micro-Ni/GO suspension was formed. The freestanding micro-Ni/GO film was prepared by filtering the above micro-Ni/GO suspension through a 0.22 µm pore-sized membrane (Millipore, USA) under vacuum. The micro-Ni/GO film can be peeled off from the membrane and then dried under vacuum for 12 h. The micro-Ni/GO film was preannealed at 300 °C for 1 h under an argon atmosphere in a tube furnace to obtain the micro-Ni/RGO film.

Preparation of Nano-Ni@C/RGO Film: The Joule heating process was conducted by applying a direct current to the mounted micro-Ni/RGO film in a vacuum chamber. The glass holder is described in the Supporting Information section of the device geometry (Figure S1d, Supporting Information). After vacuumed using turbo pump, the high-temperature self-assembly of Ni nanoparticles in RGO matrix was transiently driven by direct current using Keithley power source (Figure S1a–c, Supporting Information). The fast current pulse through the sample (width × length × thickness: 5 mm × 10 mm × 70 µm) was programed to go from 0 to 3 A with a duration of 60 ms and generated a great deal of heat. After cooling down to room temperature, the obtained film was peeled off from the glass holder for use.

Characterization Methods: The morphologies of the specimens were investigated by a Hitachi SU-70 field emission scanning electron microscope and an aberration-corrected JEOL JEM-ARM200CF STEM equipped with a 200 keV cold-field emission gun and HAADF detector. The HAADF images were obtained using a 22 mrad probe convergence angle and a 90 mrad inner detector angle. Raman spectroscopy was measured with a Horiba Yvon LabRam ARAMIS confocal Raman microscope using a 633 nm He–Ne laser. The electrical conductivity of the as-prepared film before and after the Joule heating treatment was measured with a Keithley and obtained by linearly fitting the *I–V* curve.

Temperature Measurement: To measure the temperature during the ultrafast fabrication of nanoparticles, the diagnostics should be able to deal with small, sub-millisecond time scales. To this end, the light emitting from the heated as-prepared film was collected and sent into a 0.5 m spectroscope (Acton SP 500i) with a 150 L mm^{-1} grating. The spectra were collected by a 32 channel PMT array coupled with a high-speed data acquisition system (Vertilon IQSP 580). The data were attained over the wavelength range of 513–858 nm (incorporating 27 channels of the PMT) and the system was calibrated based on a black body furnace in the range of 1200–1500 K. The sample rate on the acquisition system was set at 10 kHz. The time-resolved spectra were fitted according to the Planck's law in order to extract the temperature.

Theoretical Calculation: In order to study the adsorption of Ni or C atoms on the nanoclusters, Monte Carlo simulations were carried out with the module adsorption locator in Material Studio. The universal force field was selected with medium quality to ensure the accurate analysis. Molecular dynamics were calculated with the discover module in Material Studio, and the heating or cooling sections were realized through canonical ensemble (NVT) and micro-canonical ensemble (NVE) procedures in turn. The thermostat was chosen as Anderson, and the dynamic time was longer than 5 ps.

Electrochemical Measurements: The electrocatalytic performance of the as-prepared electrodes for H_2O_2 electro-oxidation was measured in a standard three-electrode electrochemical system with a saturated Ag/AgCl electrode as the reference electrode and Pt plate as the counter electrode. CV, chronoamperometry (CA), LSV were carried out by using a computerized potentiostat (VMP3/Z Bio-Logic) controlled by the EC-lab software. The electrolyte for testing the H_2O_2 electrocatalytic performance was a mixed solution of KOH and H_2O_2. The test temperature of electrolyte was precisely adjusted in ±1°C increments by a thermostatic water bath.

Supporting Information

Supporting Information is available from the Wiley Online Library or from the author.

Acknowledgements

Y.L. and Y.C. contributed equally to this paper. The authors acknowledge the support of the National Science Foundation (Grant No. 1635221). Y.L. acknowledges the China Scholarship Council (CSC) for financial support.

Received: August 12, 2016
Revised: November 16, 2016

---

[1] C. Wang, M. Waje, X. Wang, J. M. Tang, R. C. Haddon, Y. Yan, *Nano Lett.* **2004**, *4*, 345.
[2] L. Carrette, K. Friedrich, U. Stimming, *Fuel Cells* **2001**, *1*, 5.
[3] W. Li, X. Wang, Z. Chen, M. Waje, Y. Yan, *J. Phys. Chem. B* **2006**, *110*, 15353.
[4] F. Yang, K. Cheng, Y. Mo, L. Yu, J. Yin, G. Wang, D. Cao, *J. Power Sources* **2012**, *217*, 562.
[5] F. Yang, K. Cheng, X. Liu, S. Chang, J. Yin, C. Du, L. Du, G. Wang, D. Cao, *J. Power Sources* **2012**, *217*, 569.
[6] K. Ye, F. Guo, Y. Gao, D. Zhang, K. Cheng, W. Zhang, G. Wang, D. Cao, *J. Power Sources* **2015**, *300*, 147.
[7] L. An, T. Zhao, X. Yan, X. Zhou, P. Tan, *Sci. Bull.* **2015**, *60*, 55.
[8] A. Aytaç, M. Gürbüz, A. E. Sanli, *Int. J. Hydrogen Energy* **2011**, *36*, 10013.

[9] F. Yang, K. Cheng, T. Wu, Y. Zhang, J. Yin, G. Wang, D. Cao, *RSC Adv.* **2013**, *3*, 5483.
[10] M. R. Miah, T. Ohsaka, *Electrochim. Acta* **2009**, *54*, 1570.
[11] J. Li, Q. Yu, T. Peng, *Anal. Sci.* **2005**, *21*, 377.
[12] M. Honda, T. Kodera, H. Kita, *Electrochim. Acta* **1983**, *28*, 727.
[13] S.-i. Yamazaki, Z. Siroma, H. Senoh, T. Ioroi, N. Fujiwara, K. Yasuda, *J. Power Sources* **2008**, *178*, 20.
[14] F. Yang, K. Cheng, T. Wu, Y. Zhang, J. Yin, G. Wang, D. Cao, *Electrochim. Acta* **2013**, *99*, 54.
[15] Y. Kwon, S. J. Raaijman, M. Koper, *ChemCatChem* **2014**, *6*, 79.
[16] D. Zhang, D. Cao, K. Ye, J. Yin, K. Cheng, G. Wang, *Electrochim. Acta* **2014**, *139*, 250.
[17] D. Zhang, K. Ye, K. Cheng, Y. Xu, J. Yin, D. Cao, G. Wang, *RSC Adv.* **2014**, *4*, 17454.
[18] H. D. Jang, S. K. Kim, H. Chang, J.-H. Choi, B.-G. Cho, E. H. Jo, J.-W. Choi, J. Huang, *Carbon* **2015**, *93*, 869.
[19] D. Voiry, H. Yamaguchi, J. Li, R. Silva, D. C. Alves, T. Fujita, M. Chen, T. Asefa, V. B. Shenoy, G. Eda, *Nat. Mater.* **2013**, *12*, 850.
[20] B. Y. Xia, H. B. Wu, N. Li, Y. Yan, X. W. D. Lou, X. Wang, *Angew. Chem.* **2015**, *127*, 3868.
[21] Y. R. Zheng, M. R. Gao, Q. Gao, H. H. Li, J. Xu, Z. Y. Wu, S. H. Yu, *Small* **2015**, *11*, 182.
[22] W. Zhou, X.-J. Wu, X. Cao, X. Huang, C. Tan, J. Tian, H. Liu, J. Wang, H. Zhang, *Energy Environ. Sci.* **2013**, *6*, 2921.
[23] M. R. Berber, T. Fujigaya, K. Sasaki, N. Nakashima, *Sci. Rep.* **2013**, *3*, 1764
[24] L. Qu, L. Dai, *J. Am. Chem. Soc.* **2005**, *127*, 10806.
[25] K. Zhao, S. Zhuang, Z. Chang, H. Songm, L. Dai, P. He, Y. Fang, *Electroanalysis* **2007**, *19*, 1069.
[26] Z. Xu, Z. Li, X. Tan, C. M. Holt, L. Zhang, B. S. Amirkhiz, D. Mitlin, *RSC Adv.* **2012**, *2*, 2753.
[27] L. Zhang, L. Wang, C. M. Holt, B. Zahiri, Z. Li, K. Malek, T. Navessin, M. H. Eikerling, D. Mitlin, *Energy Environ. Sci.* **2012**, *5*, 6156.
[28] L.-R. Zhang, J. Zhao, M. Li, H.-T. Ni, J.-L. Zhang, X.-M. Feng, Y.-W. Ma, Q.-L. Fan, X.-Z. Wang, Z. Hu, *New J. Chem.* **2012**, *36*, 1108.
[29] X. Wang, H. Xue, L. Yang, H. Wang, P. Zang, X. Qin, Y. Wang, Y. Ma, Q. Wu, Z. Hu, *Nanotechnology* **2011**, *22*, 395401.
[30] C. Zhang, W. Lv, Q. Yang, Y. Liu, *Appl. Surf. Sci.* **2012**, *258*, 7795.
[31] Q. Yun, X. Qin, W. Lv, Y.-B. He, B. Li, F. Kang, Q.-H. Yang, *Carbon* **2015**, *93*, 59.
[32] S. H. Bae, J. E. Kim, H. Randriamahazaka, S. Y. Moon, J. Y. Park, I. K. Oh, *Adv. Energy Mater.* **2016**, *6*, 1601492.
[33] Y. Li, G. Wang, T. Wei, Z. Fan, P. Yan, *Nano Energy* **2016**, *19*, 165.
[34] A. C. Ferrari, D. M. Basko, *Nat. Nanotechnol.* **2013**, *8*, 235.
[35] Y. Chen, K. Fu, S. Zhu, W. Luo, Y. Wang, Y. Li, E. M. Hitz, Y. Yao, J. Dai, J. Wan, *Nano Lett.* **2016**, *16*, 3616.
[36] X. Xia, Y. Zhang, Z. Fan, D. Chao, Q. Xiong, J. Tu, H. Zhang, H. J. Fan, *Adv. Energy Mater.* **2015**, *5*, 1401709.
[37] H. J. Lee, W. Cho, E. Lim, M. Oh, *Chem. Commun.* **2014**, *50*, 5476.
[38] J. Huang, P. Xu, D. Cao, X. Zhou, S. Yang, Y. Li, G. Wang, *J. Power Sources* **2014**, *246*, 371.
[39] D. Wang, W. Yan, S. H. Vijapur, G. G. Botte, *J. Power Sources* **2012**, *217*, 498.
[40] Q. Xiao, Y. Zhang, X. Guo, L. Jing, Z. Yang, Y. Xue, Y.-M. Yan, K. Sun, *Chem. Commun.* **2014**, *50*, 13019.
[41] M. A. Hoque, F. M. Hassan, M.-H. Seo, J.-Y. Choi, M. Pritzker, S. Knights, S. Ye, Z. Chen, *Nano Energy* **2016**, *19*, 27.
[42] F. Yang, K. Cheng, X. Xue, J. Yin, G. Wang, D. Cao, *Electrochim. Acta* **2013**, *107*, 194.
[43] J. Wu, F. Hu, X. Hu, Z. Wei, P. Shen, *Electrochim. Acta* **2008**, *53*, 8341.
[44] R. Liu, X. Jiang, F. Guo, N. Shi, J. Yin, G. Wang, D. Cao, *Electrochim. Acta* **2013**, *94*, 214.
[45] D. Zhang, K. Ye, D. Cao, B. Wang, K. Cheng, Y. Li, G. Wang, Y. Xu, *Electrochim. Acta* **2015**, *156*, 102.
[46] F. Kadirgan, S. Beyhan, T. Atilan, *Int. J. Hydrogen Energy* **2009**, *34*, 4312.
[47] C. A. Angelucci, H. Varela, E. Herrero, J. M. Feliu, *J. Phys. Chem. C* **2009**, *113*, 18835.